Mapping Surface Currents and Waves with Interferometric Synthetic Aperture Radar in Coastal Waters: Observations of Wave Breaking in Swell-Dominant Conditions*

4 authors, including:

Paul Hwang
United States Naval Research Laboratory
242 PUBLICATIONS   **3,771** CITATIONS

SEE PROFILE

Mark A. Sletten
United States Naval Research Laboratory
88 PUBLICATIONS   **710** CITATIONS

SEE PROFILE

Some of the authors of this publication are also working on these related projects:

Infrared Hydrodynamics View project

Correlation time of ocean surface waves View project

Mapping Surface Currents and Waves with Interferometric Synthetic Aperture Radar in Coastal Waters: Observations of Wave Breaking in Swell-Dominant Conditions*

PAUL A. HWANG, JAKOV V. TOPORKOV, MARK A. SLETTEN, AND STEVEN P. MENK

Remote Sensing Division, Naval Research Laboratory, Washington, D.C.

ABSTRACT

Airborne and spaceborne interferometric synthetic aperture radars (InSARs) produce surface velocity measurements at very high spatial resolutions over a large area. The data allow construction of the velocity strain field for highlighting ocean surface processes such as wave breaking and rip currents. Also, coherence between signals from two interferometric channels is a descriptor of the correlation condition of the surface roughness that scatters back the radar signals and it is an indication of the ocean surface turbulence. Wave breaking is a major turbulence source causing surface roughness decorrelation, thus the coherence parameter serves as an independent means for detecting wave breaking. The results of breaking detection using roughness decorrelation and critical local acceleration are comparable. In this paper, the breaking fraction in swell-dominant mixed seas along a cross-shore transect is compared with several steepness parameters characterizing different length scales of surface waves. The highest correlation coefficient (from 0.90 to 0.99) is between the breaking fraction and windsea mean square slope contributed primarily by short waves. This result reinforces the previous field observations showing that the length scales of breaking waves are much shorter than the energetic components near the spectral peak, although dominant waves and the associated wave group modulation are important in triggering the breaking process. The large spatial coverage of airborne or spaceborne operation further offers the opportunity to investigate evolution of the surface wave spectrum in high spatial (subkilometer) resolution. This capability is very useful for monitoring the coastal wave and current environment.

1. Introduction

The coastal zone is a very dynamic region where wave and current conditions change rapidly over a short distance. The short time and length scales of variation demand a high density of sensors deployed in situ to acquire detailed measurements for characterizing the nearshore hydrodynamics. In this respect, various remote sensing techniques prove to be very valuable because they provide continuous spatial coverage over a reasonably large region to complement the in situ measurements. For example, many video and imaging radar stations have been established around the world to monitor continuously the wave condition and shoreline change in coastal regions.

Airborne and spaceborne synthetic aperture radar (SAR) systems are also capable of high spatial resolution surface wave measurements: the typical pixel size is on the order of 1 m in airborne systems and one to tens of meters in spaceborne systems. In particular, in interferometric operation, the phase difference between the signals from two antennae yields the information on the surface velocity [along-track interferometry (ATI)] or surface elevation [cross-track interferometry (XTI)]. In section 2, we present a case of applying ATI to observe the obliquely incident wave field that may lead to the formation of a rip current and longshore current along a linear beach. [The actual azimuthal resolution is further complicated by the short correlation time of the radar backscattering roughness elements, or equivalently the velocity and acceleration spread in the resolution cell during the integration time, e.g., see reviews by Plant and Keller (1983), Hasselmann et al. (1985), and Kasilingam and Shemdin (1988). As described in the

---

Corresponding author address: Dr. Paul A. Hwang, Remote Sensing Division, Naval Research Laboratory, 4555 Overlook Avenue SW, Washington, DC 20375.
E-mail: paul.hwang@nrl.navy.mil

appendix, the azimuthal resolution of the present dataset is estimated to be about 3.4 m in nonbreaking regions and 19 m in breaking regions.]

The oscillatory component of the surface current field mapped by the ATI is contributed primarily by the surface waves and it is a good source of data for the continuous mapping of the directional wave spectrum along the ground track of the flight path. Because of the relationship between surface wave elevation and surface wave orbital velocity is much better defined in comparison to the modulation transfer function that relates the wave height or wave slope to the variation in the radar backscatter intensity, derivation of the wave spectrum from radar measurements is considerably simplified by using the velocity field than the backscatter intensity field (e.g., Alpers et al. 1981; Alpers 1983; Hasselmann et al. 1985; Hasselmann and Hasselmann 1991; Marom et al. 1990, 1991; Lyzenga and Bennet 1991; Lyzenga and Malinas 1996; Bao et al. 1999; Vachon et al. 1999; He and Alpers 2003; Zhang et al. 2009; Hwang et al. 2006, 2010). An example of airborne mapping of the wave field yielding a subkilometer resolution along a cross-shore track about 20 km long is illustrated in section 3.

The coherence (γ), here defined as the absolute value of the complex correlation coefficient (Carande 1994; Franceschetti and Lanari 1999; Rosen et al. 2000; Toporkov et al. 2005) of the signals from the two antennae forming the interferometer, reflects the turbulence condition of the surface roughness patches that scatter back the radar signals. On the ocean surface, wave breaking is a primary generation source of the surface turbulence that causes the surface roughness decorrelation. From examining the coherence result, we found that γ may be used to detect surface wave breaking. Independently, the velocity gradient computed from the spatial velocity data, coupled with the wave information derived from the oscillatory velocity component, yields an estimate of the local acceleration of the surface wave field. The computed local acceleration may also be used for detecting wave breaking following the critical acceleration criterion (e.g., Longuet-Higgins and Smith 1983; Longuet-Higgins 1985; Hwang et al. 1989). These methods for breaking wave detection are described in section 4. Also presented in this section is an analysis of the correlation between the breaking fraction and different wave steepness parameters. There are several different ways of quantifying wave steepness, such as the significant slope (Huang et al. 1981), dominant wave steepness (Banner et al. 2000), and the more traditional mean square slope (Cox and Munk 1954), which can be calculated from the second moment of the wavenumber spectrum or the fourth moment of the

frequency spectrum. In our data, the wave condition is characterized by windsea propagating about perpendicular to the strong swell in a coastal region. Breaking wave analysis is performed along a cross-shore transect about 20 km long. The correlation of breaking fraction is markedly stronger with the windsea mean square slope than with other steepness parameters emphasizing the dominant waves. The implications on the wave breaking properties are presented.

A summary is given in section 5, and several issues regarding the impact of SAR imaging mechanisms on the spatial resolution and the interpretation of the interferometric synthetic aperture radar (InSAR)-derived velocity and velocity gradient fields are discussed in the appendix.

2. Surface velocity field and surf zone

An along-track interferometry (ATI) measures the ocean surface current remotely by detecting the phase difference of the radar returns from the same surface roughness patch using two receiving antennae displaced along the flight direction (Goldstein and Zebker 1987; Goldstein et al. 1989). The phase difference is produced by the Doppler frequency shift caused by the surface motion (from all sources) advecting the short surface waves (the roughness patch) that scatter back the radar signals to the receivers; the surface roughness patch serves as the tracer of these surface currents.

The phase difference ψ_{AT} is proportional linearly to the velocity component projected in the radar slant range direction, that is, the radial velocity:

$$u_r = \frac{\psi_{AT}}{4\pi} \frac{\lambda}{B_e} V_p, \qquad (1)$$

where V_p is the platform speed, and B_e is the effective baseline, which is one-half of the physical along-track antenna separation if only one antenna in the pair is transmitting. The phase difference is caused by the ocean surface motion from all sources including mean ocean currents, orbital velocities of internal or surface waves, bathymetry-induced currents, and the phase velocities of the Bragg resonance wave components that scatter back the radar waves. Special cases showing significant deviation of the phase–current relationship (1) have been presented by Thompson and Jensen (1993) and Romeiser and Thompson (2000). In the former, the group velocity of the Bragg-resonance surface waves and the phase speed of the modulating internal waves are very close. Significant overestimation of the interferometric current is found under the condition of a low wind blowing normal to the internal wave
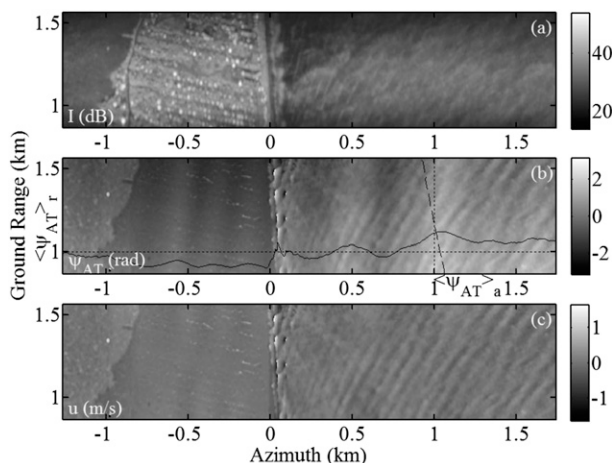
FIG. 1. An example of the SAR images of a nearshore region covering about 3 km along track (azimuth) and 0.7 km ground range: (a) the radar backscatter intensity I, (b) ATI phase ψ_{AT}, and (c) the oscillatory component of the radial velocity field u. In (b) the range mean and azimuth mean of the phase image (in unit radian) are superimposed as solid and dashed curves, scaled (divide by 10) and offset (add 1) to fit in the plotting area.

propagation direction. In the latter, surface currents with significant spatial variations are shown to be distorted in the radar interferometry. The source of discrepancy for both cases is attributable to the wave modulation effects causing nonuniform distribution of the ocean surface roughness and the associated Doppler frequency shift of the roughness elements in the SAR resolution cells. The power–velocity correlation introduces a correction proportional to the product of the modulation transfer function and the mean square slope of the modulating waves in the phase–current relationship (Romeiser and Thompson 2000). These studies suggest that surface currents inferred by radar interferometry may be distorted in conditions with steep surface waves and situations favoring strong nonlinear modulation of the Bragg surface roughness.

Figure 1 shows an example of the SAR images of a nearshore region covering about 3 km along track (azimuth) and 0.7-km ground range. Displayed in the figure are the uncalibrated radar backscatter intensity (I), ATI phase (ψ_{AT}) and the oscillatory component of the radial velocity (u). The last quantity is obtained from (1) with the residual motion effects as well as any mean surface currents removed, which is done by subtracting from u_r the range mean along each azimuth row and then subtracting the azimuth mean along each range column. The former subtraction removes some large-scale along-track oscillations and the latter removes a velocity ramp in the range direction: both are artifacts left over from the imperfect motion correction. For

illustration, the range mean and azimuth mean of the phase image, $\langle\psi_{AT}\rangle_r$ and $\langle\psi_{AT}\rangle_a$, are superimposed in Fig. 1b as solid and dashed curves, scaled (divide by 10) and offset (add 1) to fit in the plotting area. This procedure of postprocessing motion correction proves to be quite effective, although it does not remove fully the residual errors of motion compensation as evident in the sinusoidal features in the land area near azimuth -0.7 to -0.2 km in Fig. 1c. We also tried several different methods such as 1D and 2D low passing the signals with various length scales. The results in removing the residual motion effects are not as satisfactory as the subtraction of range and azimuth means as described above.

The images are acquired at about 1120 local time 20 October 2011. The average aircraft speed is 93.8 m s^{-1} and the altitude is 1217 m. The radar frequency is 9.7 GHz (X band). Three antennae are arranged in the horizontal plane such that along-track and cross-track interferometry can be performed in alternate pulses (the pulse repetition rate is 4000 Hz for each interferometry mode), that is, two antennae are in the flight direction and two are across (with one common antenna) forming a right triangle. The physical along-track spacing is 0.89 m, and the cross-track spacing is 1.07 m. The antennae are pointed at the 45° incidence angle. The system has a nominal full-bandwidth resolution of 0.3 m in azimuth and 1.2 m in range. Processed images are normally coarse grained to a 1.2 m × 1.2 m pixel size in azimuth and range, which amounts to a multilook averaging and helps reduce speckle. To improve interferometric phase estimate, the complex image product is further smoothed using a circular Gaussian window with a 6-m waist. Degrading of the azimuthal resolution due to the surface motion is discussed in the appendix; the ''actual'' azimuthal resolution is estimated to be 3.4 m in nonbreaking regions and 19 m in breaking regions.

The area covered in Fig. 1 is about 1 km south of the U. S. Army Field Research Facility (FRF) pier at Duck, North Carolina. For reference, Fig. 2a shows a map covering the experiment area with the ground track and locations of nearby wind and wave stations identified. There are two waverider buoys in the vicinity: (i) by the U.S. Army Corps of Engineers at 36.200°N, 75.714°W and local water depth 17.4 m [the data are available from the National Oceanic and Atmospheric Administration National Data Buoy Center (NDBC) archive as buoy station 44056] and (ii) by the Scripps Institution of Oceanography at 36.258°N, 75.591°W and local water depth 26 m [the wave data are available from the NDBC archive as buoy station 44110]. The information of wind speed and direction is from the NDBC archive of station DUKN7 at the Duck Pier (36.183°N, 75.747°W), owned
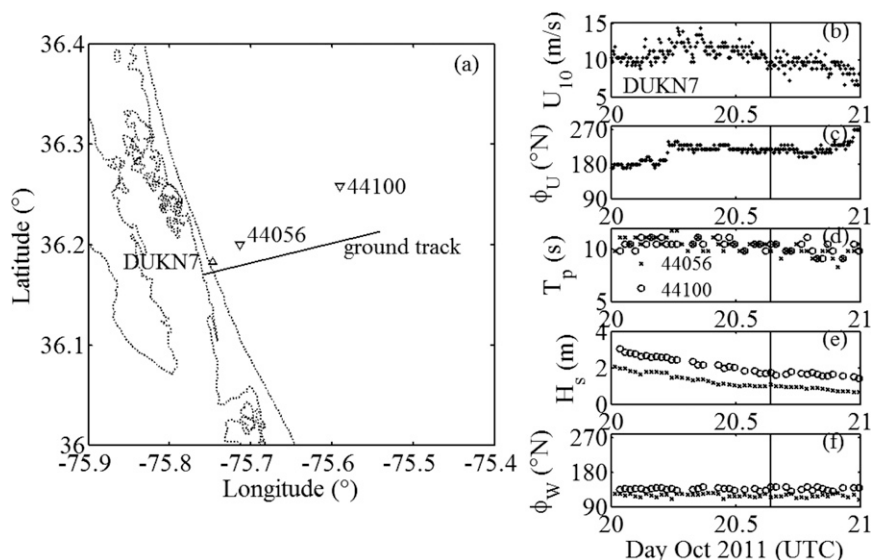
FIG. 2. (a) Area map showing the ground track and locations of in situ wind (DUKN7) and wave (44056 and 44100) stations used in this study. The relevant wind and wave conditions including (b) wind speed, (c) wind direction, (d) peak wave period, (e) significant wave height, and (f) dominant wave direction are shown to the right of the map.

and maintained by the NOAA National Ocean Service. The wind speed, wind direction, peak wave period, significant wave height, and dominant wave direction measured by the in situ wind and wave sensors are shown in Figs. 2b to 2f. The time of ATI measurements is indicated by a vertical line in each panel. Prior to the ATI data acquisition time, a relatively steady wind (10.5 ± 2 m s^{-1}) has been blowing from southwest (azimuth angle 220° from N) for more than 5 h before the SAR measurement. The wind is the residual of a storm system (wind speed reaching about 15 m s^{-1}, dominant direction from southwest) that passed through the region about 7 h earlier. The sea state is a complex combination of mixed windsea toward northeast and dominant swell from southeast. The wind direction is almost perpendicular to the dominant swell propagation direction.

Figure 3 shows a photograph taken in the same region from the aircraft at about 21 min prior to the radar data collection. North is approximately toward the top of the picture and the FRF pier is visible in the upper part of the photograph. The longer branch of the Y-shaped buildings at the lower left of the photograph—about 120 m long as measured from the Google earth overhead image—is used as the scale reference and a ruler with 50 divisions is superimposed on the photograph near the building. Calibrated with the building length, the distance between two tick marks of the ruler is about 7 m. The picture shows clearly a train of swell coming from the southeast propagating toward the coast. The waves break at some distance offshore, presumably

triggered by underwater sandbars or some other bottom features oriented almost parallel to the coastline (including parallel bathymetry). A second sequence of breaking occurs farther inshore, displaying a crescentic feature that is a signature of rip current cells (e.g., Dalrymple et al. 2011; Tiessen et al. 2011; Castelle et al. 2012). The spacing between the two breaking sequences is about 50 m. The periodic spacing of the rip current cells revealed in the crescentic feature matches that of the offshore breaking sequence. The surface features in the radar images (Fig. 1) show significant resemblance with those in

FIG. 3. A photograph covering the nearby region of Fig. 1: the photo is taken from the aircraft about 21 min prior to the radar images.
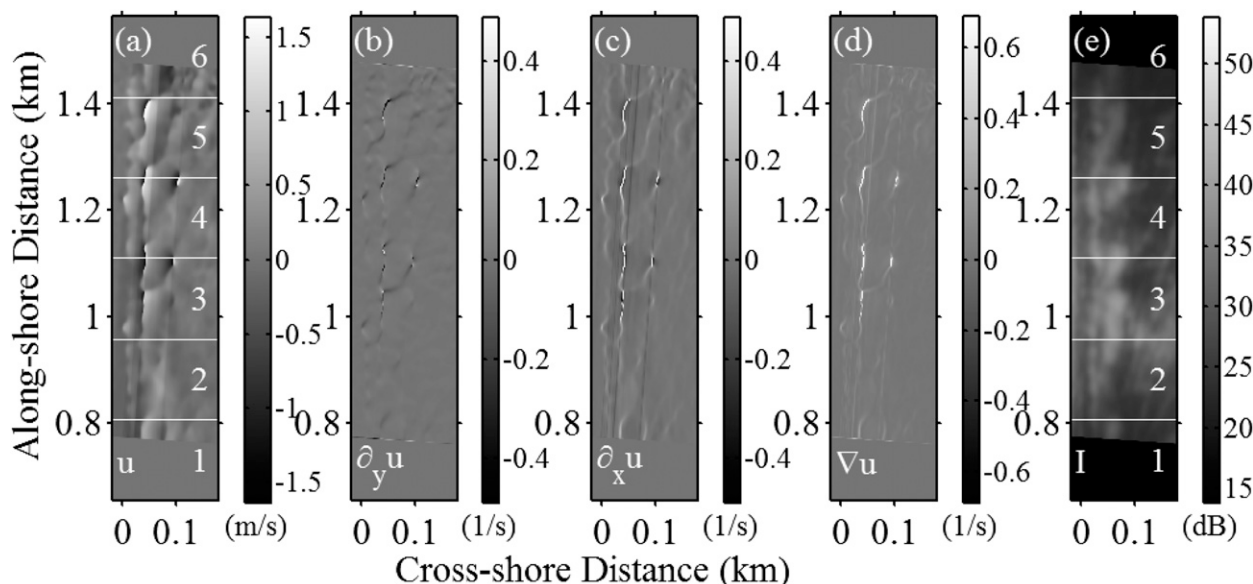
FIG. 4. The zoomed-in region of Fig. 1 near the coastline with the images rotated such that x and y axes correspond to cross-shore and alongshore directions. Breaking-induced disturbances are detectable either in the flow field (a) u, (b) $\partial_y u$, (c) $\partial_x u$, (d) $|\nabla u|$, or (e) the backscatter intensity I.

the photograph, including the two prominent breaking sequences and the periodicity of the breaking events as well as the spacing between the two breaking sequences (to be further discussed below and in Figs. 4 and 5).

With the spatial mapping of the velocity field available (here the radial component of the surface motion, u_r or u, in the look direction of the radar is measured), quantities such as the cross-shore and alongshore velocity gradients ($\partial_x u$ and $\partial_y u$, respectively) can be readily calculated. Figure 4 shows the zoomed-in coastal region, with the images rotated such that x and y axes correspond to cross-shore and alongshore directions (the rotation compensates for the 4° deviation of the flight track from the local shore normal). Breaking-induced disturbances in the flow field are clearly detectable in the images of either the velocity fields: u, $\partial_x u$, $\partial_y u$, and $|\nabla u| = [(\partial_x u)^2 + (\partial_y u)^2]^{0.5}$, or the backscatter intensity I. In this figure, the images are divided equally into six zones in the ground range direction as labeled in Figs. 4a and 4e. Based upon an inspection of the SAR intensity and velocity imagery, wave breaking seems to occur mainly in zones 3, 4, and 5 but not in zone 2. (Zones 1 and 6, which are only partially filled with wave data, are excluded in the analysis.) Figure 5 shows the decimated cross-shore transects of the radar-measured velocity strain $\partial_x u$ in areas with and without wave breaking, shown here are zone 4 and zone 2, respectively (the vertical scale for zone 2 is one tenth of that for zone 4). The result illustrates the significant modification of the flow field by wave breaking. We can approximate the

acceleration of the flow field by $\partial_t u \approx c \partial_x u$, where c is the phase velocity of the wave field. The swell period is about 10 s as recorded by the in situ buoys (Fig. 2d). The wavelength estimated from Fig. 4 is about 60 m, thus
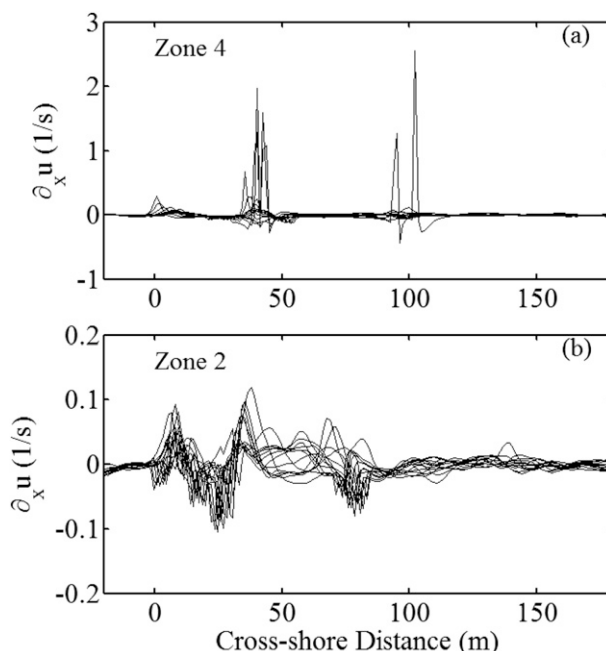

FIG. 5. Decimated cross-shore transects of the radial velocity strain $\partial_x u$ in (a) breaking areas (zones 3, 4, and 5 in Fig. 4a; shown here is zone 4), and (b) nonbreaking area (zone 2 in Fig. 4a). The vertical scale in (b) is one tenth of that in (a).

$c \approx 6$ m s^{-1} and the maximal acceleration of breaking waves exceeds $1.5g$, where g is the gravitational acceleration (Fig. 5a, showing zone 4). In contrast, the peak acceleration in the nonbreaking zone 2 is about $0.07g$ (Fig. 5b). However, care is needed in attempting to quantify the velocity gradient because of the nonlinear SAR image formation mechanisms, particularly the azimuthal shift in the image location of a moving object (the velocity bunching mechanism in wave imaging, or more generally known as the "train-off-the-track" effect in SAR imaging). The effects of velocity bunching on the measured surface velocity and the subsequent gradient computation are discussed in the appendix. Suffice it to say that significant gradients exist in regions with wave breaking (zones 3, 4, and 5) in comparison to the region without breaking (zone 2). We can make use of this SAR-observed strong gradient to detect wave breaking (section 4).

3. Wave spectrum

a. From ATI velocity spectrum to surface elevation spectrum

Techniques using the ATI-measured current field to compute surface wave spectrum have been developed since the 1990s (e.g., Marom et al.1990, 1991; Lyzenga and Bennet 1991; Goldstein et al. 1994; Lyzenga and Malinas 1996; Graber et al. 1996; Bao et al. 1999; Vachon et al. 1999; He and Alpers 2003; Hwang et al. 2006; Zhang et al. 2009). In our broadside geometry, the oscillatory portion of the radial velocity measured by the radar is related to the surface wave orbital velocity by

$$u = v_z \cos\theta_i + v_y \sin\theta_i, \qquad (2)$$

where θ_i is the radar incidence angle and v_z, v_y are the wave orbital velocity components in the vertical and ground range directions. (The z-axis points upward and the horizontal y axis is the ground range, that is, the projection of the broadside slant range on the horizontal surface.) For a wave train traveling at an angle ϕ with respect to the azimuth direction x, $v_y = v_h \sin\phi$ in which v_h is the horizontal component of the wave orbital velocity. For a spectral wave component of amplitude a, phase δ (i.e., with a complex amplitude $\eta = ae^{i\delta}$), and arbitrary water depth h, the general equations of surface orbital velocity components are (e.g., Dean and Dalrymple 1991)

$$v_h = \eta\omega\frac{\cosh kh}{\sinh kh} \quad \text{and}$$
$$v_z = -i\eta\omega. \qquad (3)$$

The phase of a progressive wave propagating in the positive (x, y) directions is defined as $\delta = k_x x + k_y y - \omega t$,

the wavenumber vector **k** can be written as (k_x, k_y) or (k, ϕ), and ω is the surface wave angular frequency.

The 2D spectrum of the radial velocity S_u is thus related to the 2D surface wave elevation spectrum S_η by

$$S_u = S_\eta\omega^2\cos^2\theta_i\left(1 + \frac{\sin^2\phi\tan^2\theta_i}{\tanh^2 kh}\right). \qquad (4)$$

For the datasets to be discussed, the surface currents are measured by a synthetic aperture radar. Because the ocean surface roughness that scatters back the radar waves is a moving target, the positions of the velocity measurements on the SAR images are not the true physical positions of the scattering roughness elements (the velocity tracer). The distortion of the velocity field produced by the nonlinear velocity bunching SAR imaging mechanism of the ocean surface has been addressed in many publications (e.g., Bao et al. 1999; Vachon et al. 1999; He and Alpers 2003; Zhang et al. 2009). He and Alpers (2003) present a detailed review of the nonlinear formulation and several different quasilinear approximations. They conclude that the following quasilinear formulation (expressed in the notations used in this paper) produces best agreement with in situ measurements

$$S_u = S_\eta\omega^2\cos^2\theta_i\left(1 + \frac{\sin^2\phi\tan^2\theta_i}{\tanh^2 kh}\right)\exp\left[-\left(\frac{k_x R}{V_p}\right)^2\sigma_{uT}^2\right], \qquad (5)$$

where R is the slant range, k_x is the wavenumber in the azimuth direction, and σ_{uT}^2 is the true radial velocity variance of the wave field, which is evaluated from the 2D surface elevation spectrum by

$$\sigma_{uT}^2 = \iint S_\eta\omega^2\cos^2\theta_i\left(1 + \frac{\sin^2\phi\tan^2\theta_i}{\tanh^2 kh}\right)k\,dk\,d\phi. \qquad (6)$$

The wave elevation spectrum can then be obtained from the ATI measured velocity spectrum through iteration.

The nonlinearity of the wave system in the ATI image can be represented by the parameter $\xi = (k_p R)^2\sigma_{uT}^2/V_p^2 \approx (k_p R)^2\sigma_u^2/V_p^2$, where k_p is the wavenumber at the spectrum peak and σ_u^2 is the ATI measured radial velocity variance. For the data presented in this paper, the typical values of the variables in the nonlinear parameter are $k_p = 0.05$ rad m^{-1}, $R = 1500$ m, $\sigma_u = 0.2$ m s^{-1}, and $V_p = 90$ m s^{-1}, so $\xi \approx 0.028$; computations show that S_η obtained from (4) and (5) differ by only about 2% for the present dataset dominated by large swell. However, for wave systems
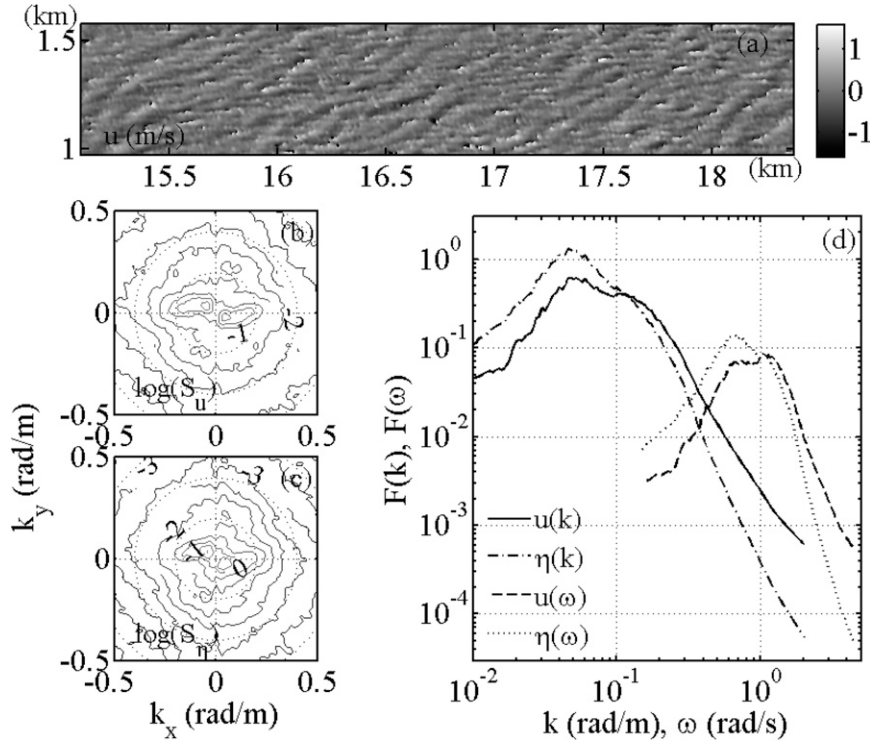
FIG. 6. An example showing the wave spectral analysis result: (a) ATI velocity field; (b) and (c) 2D velocity and displacement spectra $S_u(k_x, k_y)$ and $S_\eta(k_x, k_y)$, respectively; and (d) the directionally integrated (omnidirectional) 1D spectra $F_u(k)$, $F_\eta(k)$, $F_u(\omega)$, and $F_\eta(\omega)$.

dominated by shorter wind-generated waves, significant distortion of the directional wave spectrum may result from the strong nonlinearity (e.g., Vachon et al. 1999; He and Alpers 2003; Zhang et al. 2009).

Figure 6 illustrates the results of wave spectral analysis. Figure 6a shows the ATI velocity field; Fig. 6b and Fig. 6c are the 2D velocity and displacement spectra $S_u(k_x, k_y)$ and $S_\eta(k_x, k_y)$, and Fig. 6d displays the directionally integrated (omnidirectional) 1D spectra $F_u(k)$, $F_\eta(k)$, $F_u(\omega)$, and $F_\eta(\omega)$. The relationship between 1D and 2D spectra is

$$F(k) = \int S(k, \phi) k \, d\phi,$$

$$F(\omega) = \int S(\omega, \phi) \omega \, d\phi, \qquad (7)$$

and the relationship between wavenumber and frequency spectra is

$$F(k) dk = F(\omega) d\omega. \qquad (8)$$

The long flight track is divided into smaller segments of about 3 km each (varying between 3.0 and 3.6 km,

referred to as 3-km segments for brevity). Each spectrum is processed using a quarter of the 3-km image segments; that is, the spectrum is obtained for approximately every 0.8 km along the ground track. The wavenumber scanning distortion (encounter wavenumber) caused by the Doppler shift of the relative motion between aircraft and surface wave propagation is corrected using the algorithm of Walsh et al. (1985, 1989); see also discussions in section 4a of Hwang et al. (2000).

The 2D spectrum displays the typical 180° ambiguity commonly encountered by processing 2D stationary images. When the SAR imaging is in the linear regime (ξ small), the ambiguity can be partially resolved by using the waveform asymmetry property because the advancing phase of the surface waveform is generally steeper as a result of the ocean wave nonlinearity. The asymmetry is amplified by the differentiation process, so for a radial velocity field the calculated $\partial_x u$ and $\partial_y u$ contain the information of the dominant wave propagation direction. Particularly, for a wave propagating in $+x$ and $+y$ directions, the waveform asymmetry causes larger negative $\partial_x u$ and $\partial_y u$ (steeper forward phase), as illustrated in Figs. 7a,b. Figures 7c–f show the decimated transects of $\partial_x u$ and $\partial_y u$ of the data used for the spectra shown in Fig. 6. The results indicate that the dominant
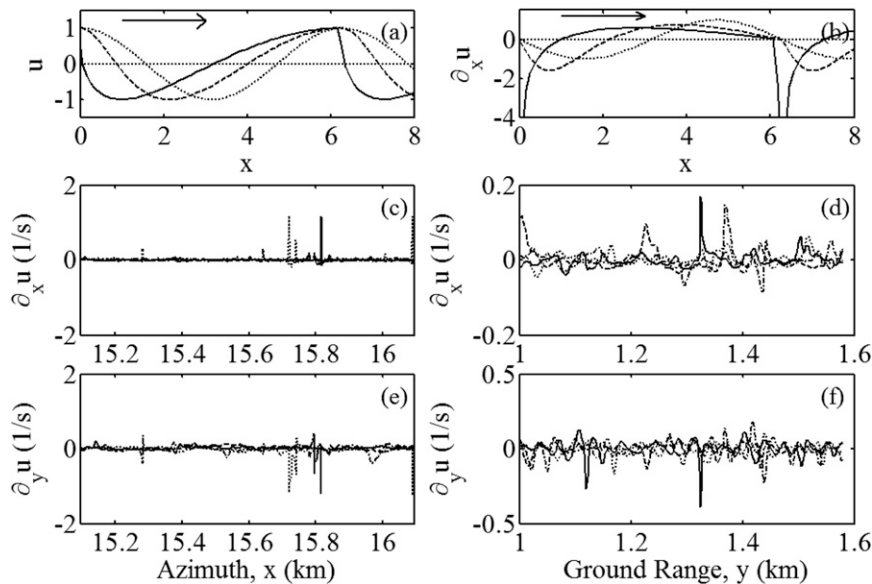
FIG. 7. An example showing the application of waveform asymmetry, which is amplified by the differentiation process in $\partial_x u$ and $\partial_y u$, to determine the dominant wave propagation direction: (a) three simulated waveforms of same wave amplitude but different nonlinearity-induced asymmetry, (b) the corresponding $\partial_x u$ amplifying the asymmetry; (c)–(f) are the $\partial_x u$ and $\partial_y u$ of the data used for the spectra shown in Fig. 6, plotted with respect to the azimuth and ground range. The results indicate that the dominant waves propagate toward $-x$ and $+y$.

waves propagate in $-x$ and $+y$ directions for this case; that is, the spectral peak is in the second quadrant of Figs. 6b and 6c.

b. Comparison with in situ and other measurements

Figure 8 shows the peak period T_p, dominant wave propagation direction ϕ_p, significant wave height H_s, and the root-mean-squared (rms) radial velocity σ_u along a cross-shore flight track covering ~20 km. As mentioned in section 2, there are two directional wave-erider buoys nearby (Fig. 2). The in situ data are shown with penta stars in Figs. 8a–c. Note that the buoy wave spectrum is typically processed from about 20 min time series of point measurements while the ATI results are based on about 81 s of data covering an area approximately 0.8 km × 0.8 km for each spectrum. The result yields subkilometer (~0.8 km) continuous spatial coverage along the flight path. The wave direction shown in Fig. 8b uses the oceanographic convention (propagation toward) with reference to east and positive counterclockwise. This can be related to the atmospheric convention (propagation from) with reference to north and positive clockwise by $\phi(°E) = 270 - \phi(°N)$. The coordinates for the 2D wave spectrum (Figs. 6b,c) are referenced to the flight track (x and k_x azimuth, y and k_y ground range). The orientation of the flight track is 15°E, which is included in Fig. 8b. The wave period and propagation direction based on the ATI data are in very

good agreement with the buoy measurements (Figs. 8a and 8b), but the ATI-measured velocity variance seems to be too low in comparison to the buoy observed wave height (Fig. 8c). For the offshore buoy location the ATI-retrieved H_s is about 0.75 of the buoy H_s whereas for the nearshore buoy location the ATI-retrieved H_s is about 0.55 of the buoy H_s. However, we note that the analysis results of similar airborne measurements presented by Vachon et al. (1999), He and Alpers (2003), and Zhang
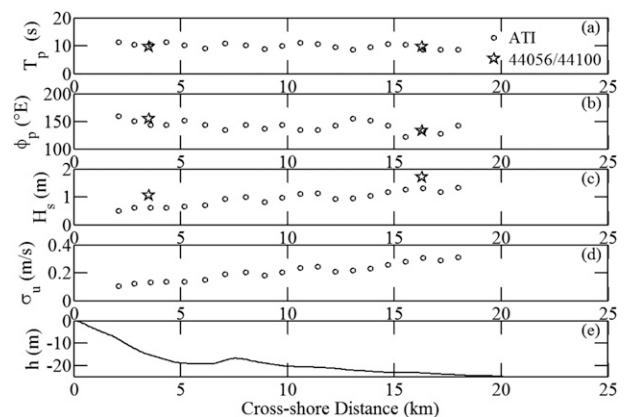

FIG. 8. (a) The peak period T_p, (b) dominant wave propagation direction ϕ_p, (c) significant wave height H_s, (d) rms radial velocity σ_u, and (e) water depth h, along a cross-shore flight track covering about 20 km. The results of in situ buoy measurements are shown with penta stars in (a)–(c).
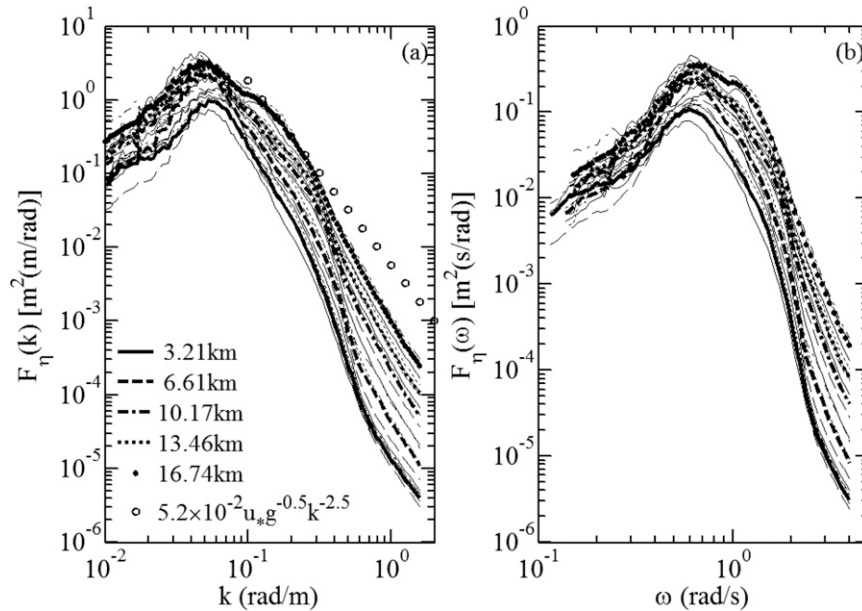
FIG. 9. Spatial evolution of the (a) wavenumber and (b) frequency spectra as measured by the ATI along a cross-shore flight track. Thin lines show the result of 0.8-km resolution, and thick lines show the 3-km resolution. The average distance from shore (km) for the 3-km result is given in the figure legend. The windsea portion of the spectrum grows with fetch and approaches the equilibrium spectrum (circles) at the far end of the flight track. The swell portion of the spectrum decays shoreward as a consequence of shoaling dissipation.

et al. (2009) show considerably better agreement (mostly within about 10% to 20% of the buoy measurements). We are unable to identify the sources of discrepancy in our measurements or data processing at this stage. In the following analyses, the variance of the spectral level is adjusted by a factor equal to the average of the two ATI/buoy ratios (1.6 for amplitude and 2.56 for variance or spectral density); the adjustment is applied to the full flight track.

Figure 9 shows the spatial evolution of the wave spectrum along the cross-shore track. As described earlier, the long track is divided into short segments about 3 km long. Four spectra are calculated from each 3-km segment. The set of thin curves represents the result of 0.8-km resolution and the set of thick curves represents the average over each 3-km segment. The mean distance from shore for each 3-km segment is shown in the figure legend. In the omnidirectional spectra shown in Fig. 9, the swell peak of the wavenumber spectrum clearly moves to higher wavenumbers as the fetch (and water depth) decreases while the swell peak of the frequency spectrum is constant. These features are expected because during shoaling the wavelength decreases while the wave period remains the same. The wave energy of the dominant swell system (with k_p in the neighborhood of 0.05 rad m^{-1}) decreases shoreward as a consequence of shoaling dissipation, whereas the windsea portion (with k greater than

about 0.1 rad m^{-1}) shows a steady growth with fetch and gradually approaches the equilibrium asymptote (e.g., Toba 1973; Phillips 1985; Hwang et al. 2000)

$$F_{\eta e}(k) = 5.2 \times 10^{-2} u_* g^{0.5} k^{-2.5}. \tag{9}$$

The windsea portion of the spectra can be compared to Fig. 7 of Hwang et al. (2000), which is the wavenumber spectrum of a wave field produced by a similar wind speed (10 m s^{-1}) in the same geographic area but over an essentially unlimited fetch (wind direction from the northeast) and a long duration (more than 10-h steady wind); the data are obtained by an airborne scanning lidar system that produces directly the 3D map of the surface elevation (no velocity bunching effect). The wave spectrum of the mature windsea under almost unlimited fetch and duration is described very well by the equilibrium spectrum function (9).

4. Breaking wave analysis

a. Breaking detection by decorrelation of surface roughness and local acceleration

In addition to the interferometric phase ψ, the InSAR image pair (say, q_1 and q_2) can be characterized by a coherence γ that varies from 0 to 1, with higher values

usually indicating better quality of phase estimates. In fact, both ψ and γ are parts of the cross-channel correlation coefficient χ (Carande 1994; Franceschetti and Lanari 1999; Rosen et al. 2000):

$$\chi = \frac{\langle q_1 q_2^* \rangle}{\sqrt{\langle |q_1|^2 \rangle \langle |q_2|^2 \rangle}} = \gamma \exp(i\psi). \qquad (10)$$

Several factors may reduce coherence, for example, low signal-to-noise ratios, viewing a scene from different angles, and changes on the surface during any time gap between the images (Franceschetti and Lanari 1999). Each can be characterized by its own coefficient (e.g., γ_N, γ_G and γ_T for "noise," "geometric," and "temporal" correlations mentioned above), and the overall coherence is the product

$$\gamma = \gamma_N \gamma_G \gamma_T. \qquad (11)$$

The values of the factors and the resulting coherence can be different for the along-track and the cross-track image pairs. If the noise properties of the channels are similar, $\gamma_{N,AT}$ and $\gamma_{N,XT}$ should be the same. The geometric (or baseline) decorrelation affects primarily the XTI, as it derives the height information by looking at the scene from two different incidence angles. In our case of the single-pass cross-track interferometry the two images are collected virtually simultaneously, therefore, temporal decorrelation is not an issue for the XTI data and $\gamma_{T,XT} = 1$. The ATI should not suffer from the geometric decorrelation ($\gamma_{G,AT} = 1$), as the two antennae (ideally) follow the same flight line and view the area from the same incidence angle. However, rapid changes in the scene can reduce the temporal coherence $\gamma_{T,AT}$ (and consequently, the overall along-track-pair coherence γ_{AT}) because the two ATI images are collected with a time lag by design.

We indeed see such a drop in γ_{AT} in the areas that can be identified as shoaling breakers in the SAR intensity imagery. This is illustrated in Fig. 10, showing the images of I, γ_{XT}, γ_{AT}, and $\Delta\gamma = \gamma_{XT} - \gamma_{AT}$ obtained in the vicinity of Oregon Inlet (North Carolina Outer Banks) on 2 June 2010. In these images, north is approximately toward the left, the ocean is toward east (upper parts of the images), and the lower halves of the images contain some land. The inlet is between about 2.5 and 3.5 km on the azimuth marker. The nearshore zone with breaking is revealed in higher (brighter) scatter intensity I (Fig. 10a). The values of γ_{XT} (Fig. 10b) in the concurrent cross-track imagery for the same breaking regions remain high (brighter) whereas those of γ_{AT} (Fig. 10c) in the concurrent along-track imagery for the same
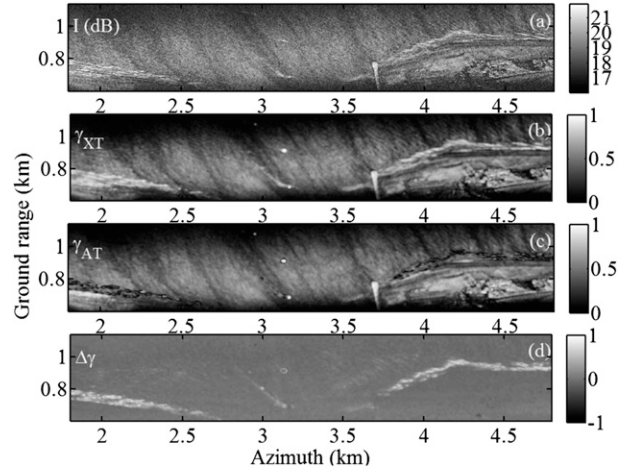

FIG. 10. Breaking wave detection of shoaling waves near Oregon Inlet using the property of surface roughness decorrelation as reflected in the coherence parameter of along-track and cross-track signals: (a) I, (b) γ_{XT}, (c) γ_{AT}, and (d) $\Delta\gamma = \gamma_{XT} - \gamma_{AT}$.

breaking regions are low (darker), confirming that the temporal decorrelation is the major contributor in the ATI coherence decline. Consequently, an approach can be devised to identify regions of severe surface roughness decorrelation (and for the ocean surface, these would be breakers with their high turbulence). In a simple case when cross-track baseline decorrelation is small (e.g., when surface undulations are relatively minor), just taking a difference between γ_{XT} and γ_{AT} (Fig. 10d) can highlight the high-turbulence regions while excluding "false alarms" in the low-signal areas (e.g., the far range region and nulls in the antenna pattern in the near range region as shown in Figs. 10b and 10c) because the low coherence in low-signal areas will be common in both cross-track and along-track channels.

More generally, to identify possible turbulent features one first looks for drops in the ATI coherence by comparing γ_{AT} to a certain threshold. The regions where the coherence is weak because of low signal-to-noise ratio (rather than due to temporal decorrelation) are then ruled out by examining the concurrent cross-track coherence; only the selected features with high γ_{XT} are retained. SAR intensity imagery (I) is another source for confirming that low signal-to-noise ratio is not the cause of the drop in the along-track coherence.

Figure 11 is an example of detecting breaking waves by the coherence method in the open ocean away from the coastal region. The top row shows I, γ_{AT}, and thresholded $\Delta\gamma$. For comparison, the bottom row illustrates the corresponding result from using the local acceleration field as described in section 2; here the images of ψ_{AT}, $|\nabla u|$, and the thresholded $|\nabla u|$ are displayed. Areas of possible wave breaking—bright spots in
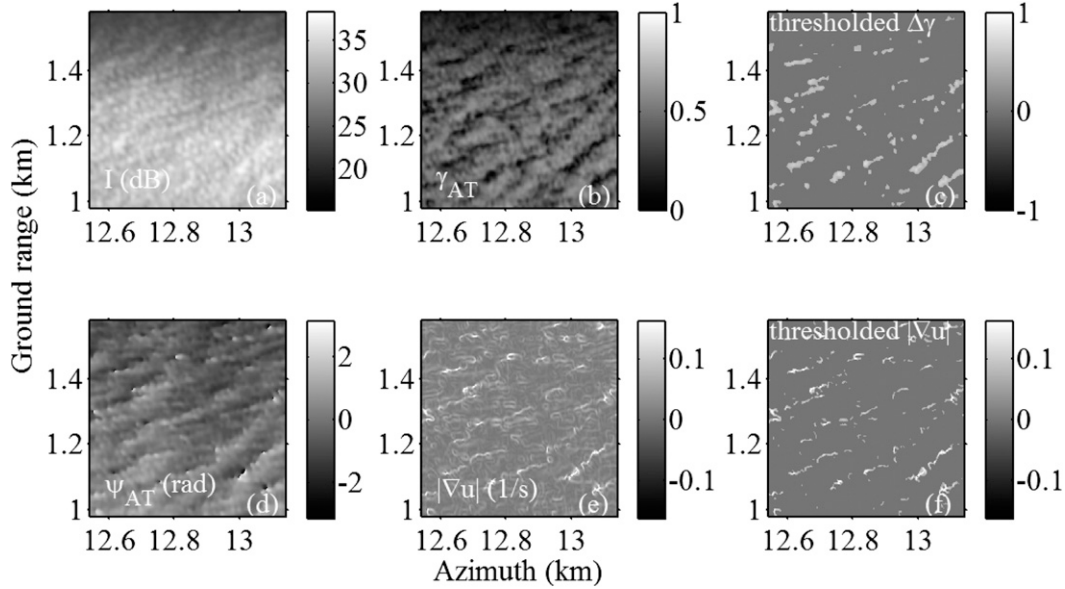
FIG. 11. Breaking wave detection in the open ocean by surface roughness decorrelation approach and comparison with local acceleration method from velocity gradient computation: (a) I, (b) γ_{AT}, (c) thresholded $\Delta\gamma$, (d) ψ_{AT}, (e) $|\nabla u|$, and (f) thresholded $|\nabla u|$.

Fig. 11c and Fig. 11f—detected by the two different methods show significant similarities. Notably, the spatial distribution of the breakers exhibits a periodicity consistent with that of the dominant waves. The general quasi-linear breaking features of northeast–southwest orientation are in accord with the surface wave pattern manifested in the surface velocity field (Fig. 11d).

b. Breaking in swell-dominant conditions

Applying the breaking detection to the full flight track described in section 3, the cross-shore distribution of the breaking fraction f_b is shown in Fig. 12a. The quantitative result depends obviously on the threshold setting of the breaking detection procedure. Here two empirical
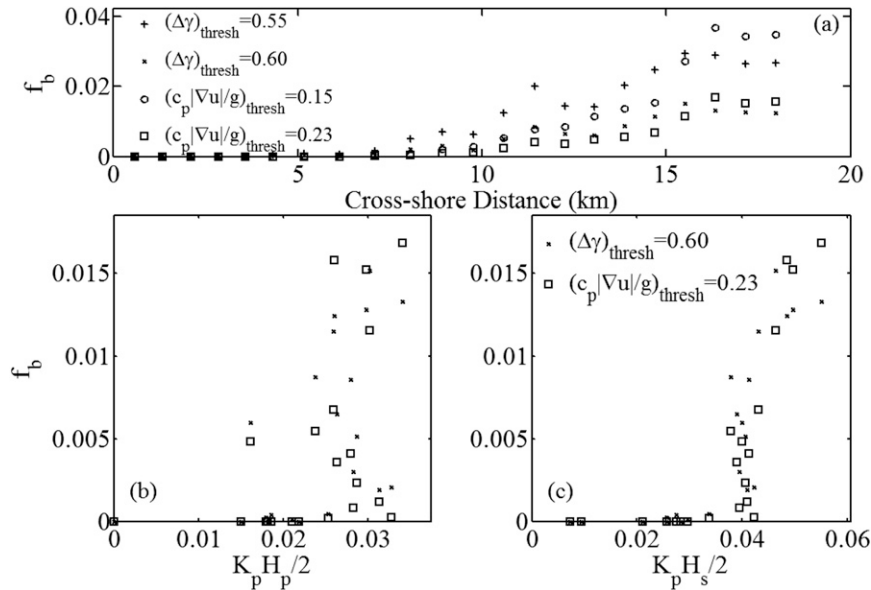

FIG. 12. (a) Spatial evolution of the fraction of wave breaking as measured by the SAR along a cross-shore flight track. Results from using the coherence method and velocity gradient method with two sets of empirical thresholds are shown. The fraction of wave breaking as a function of (b) dominant wave steepness, and (c) significant wave slope.

thresholds are shown for each of the two methods: coherence $(\Delta\gamma)_{\text{thresh}} = 0.55$ and 0.60; and velocity gradient $(c_p|\nabla u|/g)_{\text{thresh}} = 0.15$ and 0.23. Based on comparison with whitecap observations [e.g., see datasets summarized in Fig. 6 of Hwang and Sletten (2008)], the results using the higher threshold values seem to be more realistic. The data of breaking fraction are listed in Table 1 with relevant wave parameters to be discussed in the remainder of this section.

Regardless of the threshold level, the detected breaking fraction shows the characteristic of rapid increase after some distance from shore (about 7 km). This feature is consistent with the frequently observed rapid increase of related wave breaking properties (e.g., breaking probability, whitecap coverage, energy dissipation rate) when the dependent variable, such as wind speed or characteristic wave slope, exceeds a certain threshold (e.g., Dold and Peregrine 1986; Banner and Peregrine 1993; Banner et al. 2000; Hwang 2009). Based on the consideration that the nonlinear hydrodynamic processes associated with wave groups are more fundamental to the wave breaking process, Banner et al. (2000) suggest that the significant wave slope $k_p H_s/2$ (Huang et al. 1981) is an appropriate parameter for characterizing the nonlinear group behavior, here k_p is the wavenumber of the spectral peak frequency f_p computed by the dispersion relationship. Defining a dominant wave steepness $k_p H_p/2$, where H_p is an equivalent significant wave height integrated from the wave spectrum around the spectral peak from 0.7 to 1.3 f_p, they present data showing that $k_p H_p/2$ is strongly correlated with the probability of dominant wave breaking b_T.

Figure 12b shows the scatterplot of $f_b(k_p H_p/2)$, the result highlights very well the ''threshold'' characteristic of switching on/off of the breaking events. For our swell-dominant condition, the threshold is at about $k_p H_p/2 = 0.02$. For the Lake Washington and the Black Sea data (both windsea dominant) analyzed by Banner et al. (2000), the threshold level is about 0.055 for b_T; they also list two very interesting Southern Ocean mature sea cases showing very few to no breaking in high winds and high waves ($U_{10} = [19.8, 16 \text{ m s}^{-1}]$, $H_s = [9.2, 4.2 \text{ m}]$, $U_{10}/c_p = [0.94, 0.85]$, $k_p H_p/2 = [0.083, 0.050]$, $b_T = [0.027, 0]$, see their Table 2). The lowered threshold level in the present dataset probably reflects the promotion of short-scale wave breaking by the background swell, for example, through the process of swell orbital velocity modulation of shorter waves (Phillips and Banner 1974; Banner and Phillips 1974). Banner et al. (2000) show that the correlation coefficient between b_T and $k_p H_p/2$ is quite high (about 0.8). For our swell-dominant case, however, the correlation between f_b and $k_p H_p/2$ is rather

poor: 0.42 and 0.19, respectively, for f_b by coherence method and velocity gradient (or critical acceleration) method (when distinction is needed, the two breaking fractions are denoted by $f_{b\Delta\gamma}$ and $f_{b\nabla u}$, respectively). Figure 12c shows the scatterplot of the breaking fraction as a function of the significant slope, that is, $f_b(k_p H_s/2)$, where H_s is the significant wave height integrated over the full spectrum. The correlation coefficient improves to 0.83 and 0.89, but there is considerable ambiguity of the f_b values at $k_p H_s/2 \approx 0.04$. Table 2 lists the correlation coefficients and the slopes and intercepts of the linear fitting functions for the various combinations of breaking fractions and wave steepness parameters. (In this paper, the correlation coefficient is calculated for data pairs with $f_b > 10^{-4}$).

Although the application of the significant slope $k_p H_s/2$ or the dominant wave steepness $k_p H_p/2$ brings out the threshold feature of wave breaking very nicely, its use for correlating the breaking probability or breaking fraction can be questioned because the length scales of the breakers are much shorter than the dominant waves. For example, Frasier et al. (1998) present feature tracking of breaking surface waves using a high spatial- and temporal-resolution focused phased array imaging radar. Hwang et al. (2008) perform Doppler analysis of radar sea spikes that are closely associated with wave breaking. Both sets of radar investigation of surface wave breaking show that the distribution of breaking wave speed is narrow banded, the average is between about 2 and 3 m s^{-1} in both windsea and mixed seas with wind speeds between 5 and 15 m s^{-1}. Hwang (2009) describes an approach of estimating the air–sea energy transfer velocity from the energy dissipation rate function of breaking windseas and the similarity relationship of the ocean surface drag coefficient established by wavelength scaling. Applying the analysis method to the field data of mature ocean waves (Felizardo and Melville 1995) and young seas in a lake (Terray et al. 1996), the energy transfer velocity is also found to be distributed over a narrow range between 1.5 and 3 m s^{-1} for wind speeds up to 16 m s^{-1}. Field measurements of surface waves with wavenumber resolution (Banner et al. 1989; Hwang and Wang 2004) show a weak wind speed dependence of the spectral density in the range of wavelengths between about 0.2 to 2 m. As discussed in Hwang and Wang, according to the Phillips (1984) spectral source function analysis, a sluggish response of the wave spectral density to persistent wind forcing is suggestive of strong energy dissipation in the wave components of those wavelength scales.

The properties of short waves are represented more satisfactorily by the mean square slope (e.g., Cox and Munk 1954). The wind speed in our dataset is about

TABLE 1. Relevant parameters of wave breaking analysis.

x (km)	h (m)	f_{bVy}	f_{bVu}	T_p (s)	k_p (rad m⁻¹)	H_s (m)	H_p (m)	k_{rm} (rad m⁻¹)	H_{rm} (m)	k_{rw} (rad m⁻¹)	H_{rw} (m)	k_{rs} (rad m⁻¹)	H_{rs} (m)	ω_{raw} (rad s⁻¹)	H_{raw} (m)	ω_{ras} (rad s⁻¹)	H_{ras} (m)	$10^4 s_m^2$	$10^4 s_w^2$	$10^4 s_s^2$	$10^4 s_{ow}^2$	$10^4 s_{os}^2$
2.09	8.3	0.0000	0.0000	10.9	0.055	0.81	0.57	1.276	0.007	0.172	0.31	0.059	0.751	0.855	0.82	0.671	0.769	0.054	1.739	1.228	2.331	0.782
2.84	12.2	0.0000	0.0000	9.9	0.061	0.98	0.76	1.276	0.007	0.171	0.36	0.065	0.908	0.862	0.99	0.705	0.931	0.047	2.353	2.164	3.487	1.391
3.59	15.2	0.0000	0.0000	11.0	0.054	0.98	0.70	1.275	0.008	0.171	0.41	0.061	0.890	0.885	0.99	0.686	0.916	0.070	3.023	1.835	3.906	1.209
4.33	17.4	0.0002	0.0000	11.0	0.054	0.98	0.69	1.276	0.008	0.175	0.42	0.061	0.885	0.905	0.99	0.684	0.909	0.069	3.406	1.827	4.276	1.181
5.16	18.9	0.0004	0.0000	11.1	0.047	1.05	0.71	1.276	0.009	0.173	0.47	0.060	0.932	0.936	1.06	0.718	0.949	0.077	4.108	1.971	5.572	1.557
6.13	19.2	0.0001	0.0000	10.0	0.054	1.13	0.80	1.276	0.010	0.178	0.50	0.062	1.010	0.944	1.14	0.729	1.028	0.107	4.838	2.441	6.684	1.945
7.09	17.7	0.0004	0.0002	10.9	0.048	1.48	1.11	1.269	0.018	0.192	0.58	0.057	1.351	0.920	1.48	0.682	1.366	0.326	7.717	3.655	10.238	2.630
8.05	17.3	0.0021	0.0003	10.0	0.054	1.61	1.25	1.269	0.014	0.185	0.63	0.058	1.474	0.912	1.62	0.696	1.491	0.196	8.513	4.627	11.761	3.390
8.92	18.9	0.0030	0.0008	8.8	0.062	1.31	0.94	1.269	0.018	0.194	0.67	0.063	1.113	1.040	1.31	0.748	1.131	0.337	10.591	3.057	13.156	2.607
9.76	20.0	0.0019	0.0012	9.7	0.054	1.56	1.20	1.272	0.024	0.202	0.70	0.059	1.388	0.994	1.57	0.711	1.403	0.582	12.341	4.148	15.593	3.283
10.59	20.6	0.0051	0.0023	10.5	0.048	1.77	1.26	1.265	0.030	0.208	0.81	0.057	1.571	1.010	1.78	0.700	1.589	0.897	17.596	5.001	21.498	3.933
11.42	20.9	0.0086	0.0041	10.5	0.048	1.81	1.23	1.271	0.039	0.214	0.86	0.060	1.575	1.048	1.81	0.720	1.595	1.500	21.324	5.488	25.773	4.459
12.24	21.3	0.0065	0.0036	9.5	0.054	1.49	1.00	1.269	0.033	0.214	0.78	0.061	1.256	1.093	1.49	0.742	1.270	1.075	17.455	3.664	20.721	3.177
13.06	22.1	0.0060	0.0048	13.9	0.033	1.52	0.62	1.267	0.041	0.216	0.90	0.061	1.208	1.155	1.53	0.749	1.228	1.677	23.821	3.424	27.034	3.092
13.87	22.6	0.0087	0.0054	10.5	0.047	1.66	1.04	1.272	0.041	0.221	0.91	0.059	1.370	1.126	1.66	0.727	1.385	1.705	25.153	4.058	28.777	3.489
14.69	23.1	0.0115	0.0067	11.9	0.040	1.89	1.14	1.269	0.046	0.223	0.94	0.057	1.624	1.082	1.89	0.707	1.637	2.140	27.327	5.296	31.844	4.362
15.50	23.1	0.0151	0.0115	10.9	0.044	2.03	1.32	1.270	0.052	0.216	1.06	0.056	1.718	1.087	2.04	0.708	1.735	2.724	32.500	5.776	37.664	4.913
16.32	23.3	0.0133	0.0168	10.2	0.048	2.10	1.30	1.269	0.065	0.223	1.24	0.063	1.662	1.173	2.10	0.760	1.687	4.252	47.877	6.794	54.452	6.188
17.15	23.8	0.0128	0.0152	9.0	0.057	1.90	1.14	1.270	0.070	0.232	1.21	0.063	1.442	1.231	1.91	0.764	1.466	4.876	49.054	5.135	54.243	4.770
17.97	24.2	0.0124	0.0158	11.7	0.040	2.12	1.14	1.271	0.063	0.219	1.26	0.060	1.687	1.163	2.13	0.737	1.708	4.004	48.064	6.326	54.025	5.606

TABLE 2. Correlation coefficient (C), slope (a), and intercept (b) of linear fitting function for the various combinations of breaking fractions and wave steepness parameters.

	C	a	$10^4 b$
$f_{b\Delta\gamma}(k_p H_p)$	0.42	0.42	-47.30
$f_{bvu}(k_p H_p)$	0.19	0.25	-6.12
$f_{b\Delta\gamma}(k_p H_s)$	0.83	0.56	-160.52
$f_{bvu}(k_p H_s)$	0.89	0.96	-348.74
$f_{b\Delta\gamma}(s_s^2)$	0.83	29.73	-63.50
$f_{bvu}(s_s^2)$	0.77	40.96	-130.98
$f_{b\Delta\gamma}(s_w^2)$	0.92	3.11	-2.56
$f_{bvu}(s_w^2)$	0.99	4.06	-37.99
$f_{b\Delta\gamma}(s_m^2)$	0.90	30.16	16.51
$f_{bvu}(s_m^2)$	0.98	38.15	-8.22
$f_{b\Delta\gamma}(s_{\omega s}^2)$	0.81	26.73	-63.93
$f_{bvu}(s_{\omega s}^2)$	0.76	38.56	-140.99
$f_{b\Delta\gamma}(s_{\omega w}^2)$	0.92	2.92	-11.17
$f_{bvu}(s_{\omega w}^2)$	0.99	3.90	-52.49

10 m s^{-1}, so we integrate the wavenumber spectrum from $k_1 = 0.1 \text{ rad m}^{-1}$ to the upper bound $k_u = 1.6 \text{ rad m}^{-1}$ to obtain the windsea mean square slope (the phase speed of $k = 0.1 \text{ rad m}^{-1}$ wave component is 9.8 m s^{-1} at 25 m water depth):

$$s_w^2 = \int_{k_1}^{k_u} k^2 F_\eta(k)\, dk. \qquad (12)$$

For convenience, we also compute two reference quantities for characterizing the mean square slope in place of the wave spectrum:

$$H_{rw} = 4\left(\int_{k_1}^{k_u} F_\eta(k)\, dk\right)^{1/2}, k_{rw} = \left(\frac{\int_{k_1}^{k_u} k^2 F_\eta(k)\, dk}{\int_{k_1}^{k_u} F_\eta(k)\, dk}\right)^{1/2}. \qquad (13)$$

To a good approximation, the windsea mean square slope can be calculated by

$$s_w^2 \approx \left(k_{rw}\frac{H_{rw}}{4}\right)^2. \qquad (14)$$

The mean square slope of the swell portion of the wave spectrum can be computed in a similar fashion by changing the integration limits to $k_0 = 0.01 \text{ rad m}^{-1}$ and k_1 (0.01 rad m^{-1} is the lower bound of our spectrum resolution). These swell quantities are represented by s_s^2, k_{rs}, and H_{rs}. To further emphasize the short length scale of the breaking waves, we also process the corresponding steepness properties in the wave spectrum with

$k > 1 \text{ rad m}^{-1}$; these are represented by s_m^2, k_{rm}, and H_{rm} (subscript m for minilength scale waves within the spectrum, or mini waves for brevity).

If the wavenumber spectrum is not available, the windsea mean square slope can be approximated from the fourth moment of the frequency spectrum by

$$s_{\omega w}^2 \approx \frac{m_{4\omega w}}{g^2}; \quad m_{4\omega w} = \int_{\omega_1}^{\omega_u} \omega^4 F_\eta(\omega)\, d\omega. \qquad (15)$$

The corresponding reference wave height and wave frequency are

$$H_{r\omega w} = 4\left(\int_{\omega_1}^{\omega_u} F_\eta(\omega)\, d\omega\right)^{1/2}, \omega_{r\omega w} = \left(\frac{\int_{\omega_1}^{\omega_u} \omega^4 F_\eta(\omega)\, d\omega}{\int_{\omega_1}^{\omega_u} F_\eta(\omega)\, d\omega}\right)^{1/4}. \qquad (16)$$

In the present analysis, $\omega_1 = 1 \text{ rad s}^{-1}$ (phase speed $=9.7 \text{ m s}^{-1}$ at 25 m water depth), the lower and upper bounds of the frequency coverage are 0.1 and 4.0 rad s^{-1}. The swell portion of the mean square slope, reference wave frequency, and wave height can be computed in a similar fashion. The quantities k_{rm}, H_{rm}, k_{rw}, H_{rw}, k_{rs}, H_{rs}, s_m^2, s_w^2, s_s^2, $\omega_{\omega w}$, $H_{r\omega w}$, $\omega_{r\omega s}$, $H_{r\omega s}$, $s_{\omega w}^2$, and $s_{\omega s}^2$ are listed in Table 1.

Figures 13a–c show the cross-shore variation of the swell and windsea reference wave heights, wavenumbers, and mean square slopes. The windsea components show monotonic cross-shore variations whereas the swell components display some large-scale oscillations, which are probably the result of swell-bottom interactions such as bottom scattering and beating caused by the interaction of incident and reflected long waves. Figure 13d shows the cross-shore variation of the breaking fraction f_b, and Figs. 14a–c show the scatterplots of $f_b(s_s^2)$, $f_b(s_w^2)$, and $f_b(s_m^2)$. It is clear that the correlation between breaking fraction and the windsea or mini-wave mean square slopes is considerably higher than the swell counterparts, the functional dependence of $f_b(s_w^2)$ or $f_b(s_m^2)$ is also much more monotonic than that of $f_b(s_s^2)$. The correlation coefficients between f_b and s_w^2 or s_m^2 are between 0.90 and 0.99 for the various combinations of breaking detection methods and mean square slope computations (Table 2).

Noticeably, the breaking fraction dependence on the mean square slope shows a saturation trend (Figs. 14b,c), this reflects the fetch-limited growth saturation of short wave components farther offshore (Fig. 13c). Based on our experience with the scatterometer, which measures wind speed by the radar backscatter from
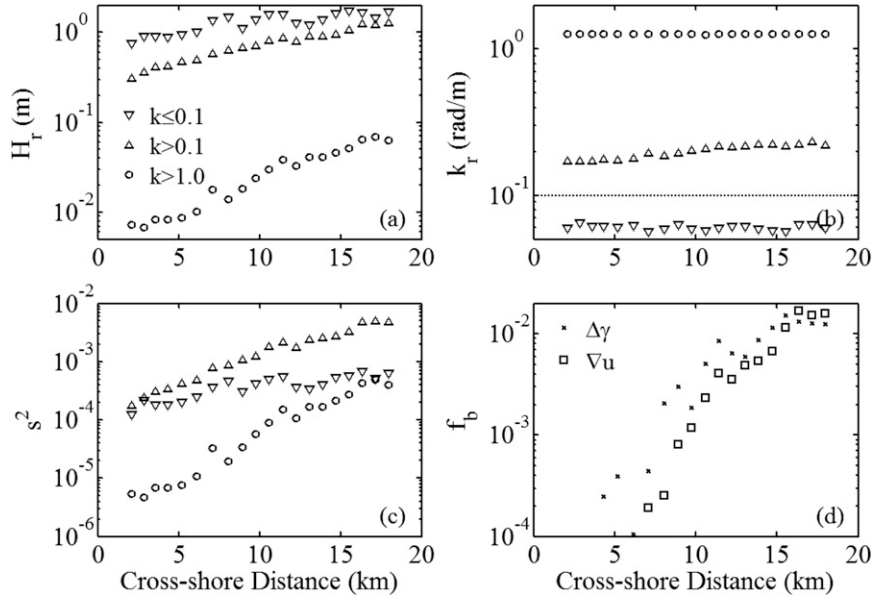
FIG. 13. Cross-shore variation of (a) H_r; (b) k_r; (c) s^2 for the wave components in the wavenumber bands of swell ($k \leq 0.1$ rad m^{-1}), windsea ($k > 0.1$ rad m^{-1}), and miniwave ($k > 1$ rad m^{-1}); and (d) f_b.

a narrow wavenumber band of short-scale water surface waves, the saturation level of waves for a given length scale is wind speed dependent (up to some wind speed, possibly about 50 m s^{-1}; this remains a difficult subject for both theoretical and experimental studies). Obviously, seeking the dependence of wave breaking properties on mean square slope becomes not very useful for the situation of almost constant wind speeds when the wave steepness reaches saturation.

5. Summary

Wave conditions in coastal regions change rapidly in relatively short distances. Airborne and spaceborne remote sensing represent a powerful means for monitoring the sea state conditions in a region covering tens to hundreds of kilometers from the shoreline. For many decades, 2D (k_x, k_y) and 3D (k_x, k_y, ω) spectra have been retrieved from the backscatter intensity of imaging
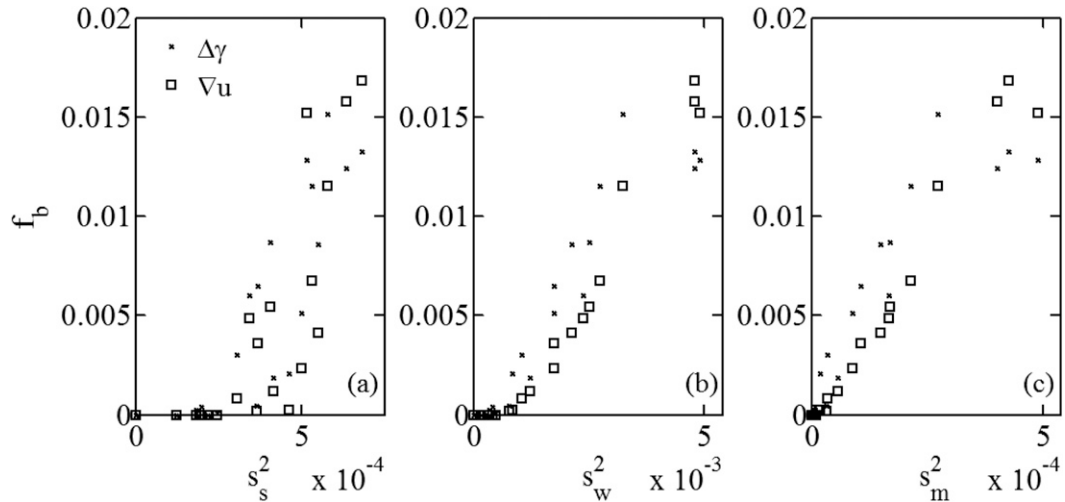

FIG. 14. Breaking fraction as a function of mean square slope: (a) swell components, (b) windsea components, and (d) miniwave components.

radars. The retrieved wavelength and wave propagation direction are generally quite accurate for real-aperture imaging radars, but the derivation of wave height from the radar backscattering intensity relies on the modulation transfer function, which depends on many factors such as the radar wavelength, incidence angle, azimuth angle, range, surface wave wavelength, period and height, water depth, wind speed, wind direction, surface currents (speed and direction), and air–sea stability conditions.

With coherent radars, the backscatter includes both magnitude and phase. In along-track interferometry, the interchannel phase difference (ψ_{AT}) is related to the surface velocity. On the ocean surface, the oscillatory component of the velocity is produced primarily by the ocean surface wave motion. Conversion of the surface wave velocity spectrum to the surface wave elevation spectrum is much more deterministic. Subkilometer spatial resolution of the evolution of surface wave spectrum can be accommodated with airborne and high-resolution spaceborne ATI (sections 2 and 3).

The spatial field of surface velocity data allows computations of the velocity strain field or the spatial gradient of the surface current. Coupled with the wave information, the velocity gradient is convertible to the local acceleration field for detecting surface wave breaking over a large area of the sea surface. The coherence between the signals from a pair of radar antennae contains valuable information on the turbulence condition of the surface roughness patch that scatters back the microwave. Particularly, γ_{AT} shows a conspicuous decrease in regions suspected of wave breaking. Breaking detections using the properties of surface roughness decorrelation and critical acceleration produce comparable results. We have applied the two breaking detection methods in the analysis of breaking waves in the coastal environment. The result shows that the breaking fraction is strongly correlated to the windsea mean square slope. This is consistent with previous observations showing that the breaking length scale is considerably shorter than the dominant wavelength. The correlation coefficient is between 0.90 and 0.99 in our dataset characterized by windsea traveling perpendicular to strong swell (sections 2 and 4).

APPENDIX

Some Relevant SAR Issues

a. Azimuthal resolution

The azimuthal resolution of a SAR system for stationary scenes is (e.g., Cutrona 1970; Harger 1970; Bao et al. 1999)

$$\delta_{a1} = \frac{\lambda R}{2 V_p T_i}, \qquad (A1)$$

where T_i is the integration time. Using nominal numbers appropriate for the data presented in this paper: $\lambda = 0.03$ m, $R = 1500$ m, $V_p = 90$ m s^{-1}, $T_i = 1$ s, then $\delta_{a1} = 0.26$ m.

For SAR imaging of the ocean surface, the scattering roughness elements are nonstationary short surface waves with complex dynamic evolution, and the effective integration time T_i' should be used in place of T_i (e.g., Plant and Keller 1983; Kasilingam and Shemdin 1988):

$$\frac{1}{T_i'^2} = \frac{1}{T_i^2} + \frac{1}{T_c^2}, \qquad (A2)$$

where T_c is the correlation time of the scattering roughness. Based on field measurements of X and Ka bands (10 and 35 GHz) radar backscatter from the ocean surface, Plant et al. (1994) suggest that T_c is about 10 ms for X band and 3 ms for Ka band. If $T_i' = 10$ ms is adopted, then the resolution degrades by a factor of about 100, to $\delta_{a1}' = 26$ m. The wave period of the Bragg resonance waves at X band (45° incidence angle) is 79 ms (wavelength 0.018 m). We feel that the decorrelation time of 10 ms for surface waves of 79 ms period seems to be too small. If the azimuthal resolution is indeed 26 m, the wavenumber spectra shown in Fig. 6 should have displayed a sharp drop of the spectral energy beyond the Nyquist wavenumber of $2\pi/52 = 0.12$ rad m^{-1}, which is clearly not the case here.

Another approach to quantify the azimuthal resolution is by considering the velocity and acceleration spread over the footprint and integration time; from such spatial and temporal domains the received radar signals are used to construct the SAR image. The analysis of Hasselmann et al. (1985) yields

$$\delta_{a2} = \frac{R v_o}{V_p}, \qquad (A3)$$

where v_o is a reference orbital velocity scale. If we use the measured rms orbital velocity $\sigma_u = 0.2$ m s^{-1} as a conservative estimate of v_o, and the same R and V_p

values above, then $\delta_{a2} = 3.3$ m. In addition to the orbital velocity, the acceleration of the ocean surface also introduces a smearing effect and produces an equivalent spatial resolution of

$$\delta_{a3} = \frac{Ra_o}{3^{1/2}V_p}\frac{T_i}{2}, \tag{A4}$$

where a_o is a reference acceleration scale of the wave field. In nonbreaking conditions, a_o is small, about $O(10^{-2}g)$. Using $a_o = 0.02g \approx 0.2$ m s^{-2}, then $\delta_{a3} = 0.9$ m.

Near breaking conditions, the velocity and acceleration spread over the footprint increase considerably. If $v_o = 1$ m s^{-1} and $a_o = 0.2g$ (average over the resolution cell) are used, then $\delta_{a2} = 16.7$ m and $\delta_{a3} = 9.4$ m.

The resultant azimuthal resolution is estimated by $\delta_a = (\delta_{a1}^2 + \delta_{a2}^2 + \delta_{a3}^2)^{0.5}$. Based on the above analysis, the azimuthal resolution of the data presented in this paper is ~3.4 m in nonbreaking regions and 19 m in breaking regions.

b. Distortion of velocity measurement caused by the SAR imaging mechanism

Care is needed in interpreting the SAR-measured ocean surface velocity and the derived quantities such as the velocity strain or local acceleration. In particular, the well-known azimuth shifting effect of SAR imaging of a moving target would displace the ocean surface roughness patch in the image from its true location. When the surface velocity is not uniform in space the observed velocity profile can be distorted significantly if the velocity strain is large (Sletten 2006). Using the convention that the radial velocity is positive in the increasing range direction, the azimuth shift is

$$\Delta x = -\frac{R}{V_p}u. \tag{A5}$$

The phase image $\psi_{AT}(x, y)$ is related to the "true velocity field" $u(x_0, y_0)$ by (e.g., He and Alpers 2003)

$$\psi_{AT}(x, y) = \frac{4\pi}{\lambda}\frac{B_e}{V_p}u(x_0, y_0)|_{x_0 = x + \frac{R}{V_p}u(x_0, y_0)}. \tag{A6}$$

The observed velocity field $u(x, y)$ therefore relates to the true velocity field by

$$u(x, y) = \frac{\psi_{AT}(x, y)}{4\pi}\frac{\lambda}{B_e}V_p = u(x_0, y_0)|_{x_0 = x + \frac{R}{V_p}u(x_0, y_0)}. \tag{A7}$$

The velocity strain is

$$\frac{du(x, y)}{dx} = \frac{du(x_0, y_0)}{dx_0}\frac{1}{1 - \varepsilon_0}\Big|_{x_0 = x + \frac{R}{V_p}u(x_0, y_0)}, \tag{A8}$$

where ε_0 is a distortion parameter,

$$\varepsilon_0 = \frac{du(x_0, y_0)}{dx_0}\frac{R}{V_p}. \tag{A9}$$

A countershift procedure can be developed to attempt the recovery of the true velocity strain field from the SAR image by the following:

$$\frac{du(x_0, y_0)}{dx_0} = \frac{du(x, y)}{dx}\frac{1}{1 + \varepsilon}\Big|_{x = x_0 - \frac{R}{V_p}u(x, y)}, \tag{A10}$$

where

$$\varepsilon = \frac{du(x, y)}{dx}\frac{R}{V_p}. \tag{A11}$$

Figure A1 shows three examples of computed results for sinusoidal wave fields similar to the conditions discussed in this paper: the wavelength is 130 m, water depth 26 m, wave period 9.9 s, wave height 1.0 m (left column), 2.0 m (middle column), and 4.0 m (right column). In each panel, the dash-dotted curve is the surface elevation, the solid curve is the true radial velocity (upper panels) or velocity strain (lower panels) for the configuration of 45° incidence angle and 120° wave propagation angle, the dashed curve is the azimuth-shifted radial velocity (upper panels) and velocity strain (lower panels), and the crosses are the countershifted results using the procedure described above. For the left column, the maximum and rms values of ε_0 are (0.260, 0.187); for the middle and right columns, the corresponding values are (0.521, 0.374) and (1.041, 0.747), respectively. The recovery for the first two cases (wave height 1.0 and 2.0 m, maximum radial velocity 0.297 and 0.594 m s^{-1}, maximum ε_0 0.260 and 0.521) is very good; for the last case (wave height 4.0 m, maximum radial velocity 1.187 m s^{-1}, maximum ε_0 1.041), there are waveform phases where the distortion parameter reaches or exceeds the critical condition ($\varepsilon_0 = 1$) and the significant distortion cannot be restored. Near these critical points, the SAR-imaged waveform becomes vertical (overlapped) or even folds over (Fig. A1c, dashed curve) and the velocity strain reaches infinity (Fig. A1f, dashed curve). The circles in Figs. A1c and A1f indicate the countershifted results showing a gap near the du/dx maximum where pixels are unrecoverable without interpolation (crosses).
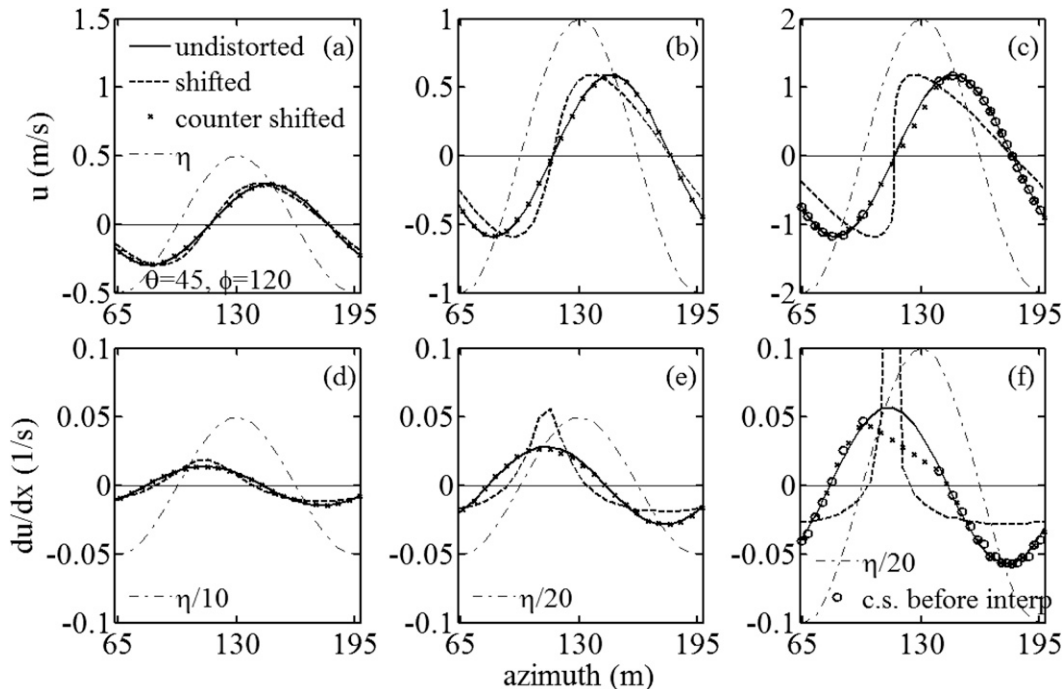
FIG. A1. Computational examples illustrating the azimuthal shift effect on SAR measured (a)–(c) velocity and (d)–(f) velocity gradient, and a countershift procedure to recover the undistorted velocity and velocity gradient fields from measured data. The wave heights are (left) 1.0, (middle) 2.0, and (right) 4.0 m. The circles in (c) and (f) indicate the countershifted results showing a gap near the maximum of du/dx reaching or exceeding the critical condition where the undistorted velocity and strain are unrecoverable without interpolation (crosses).

The critical strain can be written as (Sletten 2006)

$$\left[\frac{du(x_0, y_0)}{dx_0}\right]_{cr} = \frac{V_p}{R}. \qquad (A12)$$

For our typical flight speed (93 m s^{-1}) and slant range (1500–2000 m), the critical velocity strain is (4.6 ~ 6.0) × 10^{-2} s^{-1}. In the application of breaking detection using the velocity gradient method described in sections 2 and 4, the SAR-measured velocity and velocity strain near the breaking region are much larger than those in Fig. A1, and the measurement may be significantly distorted by the nonlinear imaging mechanism. In particular, the velocity strain frequently exceeds the critical value in regions identified as probably breaking (Figs. 5 and 11), and recovery of the true velocity strain may not be achievable. However, the location (relative to the waveform) of detected breaking and the breaking fraction determined by the gradient threshold are probably reliable.

Finally, we emphasize that the discussion presented in this appendix assumes sinusoidal flow oscillations. In near-breaking conditions, the waveform becomes severely asymmetric as a result of surface wave non-linearity, and after the breaking inception the breaking patch becomes a discrete target detached from the mother waveform that spawns the breaking patches. After reattaching to the water surface, these breaking patches would behave as free surface waves following the dispersion relationship corresponding to their length scales (Hwang 2007). Simulation of such complexity is beyond the scope of this paper, and the analysis presented here should be considered as a coarse approximation at best in near-breaking situations.

REFERENCES

Alpers, W., 1983: Monte Carlo simulations for studying the relationship between ocean wave and synthetic aperture radar image spectra. *J. Geophys. Res.,* **88** (C3), 1745–1759.

——, D. B. Ross, and C. L. Rufenach, 1981: On the detectability of ocean surface waves by real and synthetic aperture radar. *J. Geophys. Res.,* **86** (C7), 6481–6498.

Banner, M. L., and O. M. Phillips, 1974: On the incipient breaking of small scale waves. *J. Fluid Mech.,* **65,** 647–656.

——, and D. H. Peregrine, 1993: Wave breaking in deep water. *Annu. Rev. Fluid Mech.,* **25,** 373–397.

——, I. S. F. Jones, and J. C. Trinder, 1989: Wavenumber spectra of short gravity waves. *J. Fluid Mech.,* **198,** 321–344.

——, A. V. Babanin, and I. R. Young, 2000: Breaking probability for dominant waves on the sea surface. *J. Phys. Oceanogr.,* **30,** 3145–3160.

Bao, M., W. Alpers, and C. Brüning, 1999: A new nonlinear integral transform relating ocean wave spectra to phase image

spectra of an along-track interferometric synthetic aperture radar. *IEEE Trans. Geosci. Remote Sens.,* **37,** 461–466.

Carande, R. E., 1994: Estimating ocean coherence time using dual-baseline interferometric synthetic aperture radar. *IEEE Trans. Geosci. Remote Sens.,* **32,** 846–854.

Castelle, B., V. Marieu, G. Coco, P. Bonneton, N. Bruneau, and B. G. Ruessink, 2012: On the impact of an offshore bathymetric anomaly on surf zone rip channels. *J. Geophys. Res.,* **117,** F01038, doi: 10.1029/2011JF002141.

Cox, C. S., and W. Munk, 1954: Statistics of the sea surface derived from sun glitter. *J. Mar. Res.,* **13,** 198–227.

Cutrona, L. J., 1970: Synthetic aperture radar. *Radar Handbook,* M. I. Skolnik, Ed., McGraw-Hill, Inc., 23.1–23.25.

Dalrymple, R. A., J. H. MacMahan, A. J. H. M. Reniers, and V. Nelko, 2011: Rip currents. *Annu. Rev. Fluid Mech.,* **43,** 551–581.

Dean, R. G., and R. A. Dalrymple, 1991: *Water Wave Mechanics for Engineers and Scientists.* World Scientific Publishers, 353 pp.

Dold, J. W., and D. H. Peregrine, 1986: Water-wave modulation. *Proc. 20th Int. Conf. Coastal Eng.,* Taipei, Taiwan, ASCE, 163–175.

Felizardo, F., and W. K. Melville, 1995: Correlations between ambient noise and the ocean surface wave field. *J. Phys. Oceanogr.,* **25,** 513–532.

Franceschetti, G., and R. Lanari, 1999: *Synthetic Aperture Radar Processing.* CRC Press, 307 pp.

Frasier, S. J., Y. Liu, and R. E. McIntosh, 1998: Space-time properties of radar sea spikes and their relation to wind and wave conditions. *J. Geophys. Res.,* **103** (C9), 18 745–18 757.

Goldstein, R. M., and H. A. Zebker, 1987: Interferometric radar measurement of ocean surface currents. *Nature,* **328,** 707–709.

——, T. P. Barnett, and H. A. Zebker, 1989: Remote sensing of ocean currents. *Science,* **246,** 1282–1285.

——, F. Li, J. Smith, R. Pinkel, and T. P. Barnett, 1994: Remote sensing of ocean waves: The surface wave process program experiment. *J. Geophys. Res.,* **99,** 7945–7950.

Graber, H. C., D. R. Thompson, and R. E. Carande, 1996: Ocean surface features and currents measured with synthetic aperture radar interferometry and HF radar. *J. Geophys. Res.,* **101,** 25 813–25 832.

Harger, R. O., 1970: *Synthetic Aperture Radar Systems.* Academic Press, 240 pp.

Hasselmann, K., and S. Hasselmann, 1991: On the nonlinear mapping of an ocean wave spectrum into a synthetic aperture radar image spectrum and its inversion. *J. Geophys. Res.,* **96** (C6) 10 713–10 729.

——, R. K. Raney, W. J. Plant, W. Alpers, R. A. Shuchman, D. R. Lyzenga, C. L. Rufenach, and M. J. Tucker, 1985: Theory of synthetic aperture radar ocean imaging: A MARSEN view. *J. Geophys. Res.,* **90** (C3) 4659–4686.

He, Y., and W. Alpers, 2003: On the nonlinear integral transform of an ocean wave spectrum into an along-track interferometric synthetic aperture radar image spectrum. *J. Geophys. Res.,* **108,** 3205, doi:10.1029/2002JC001560.

Huang, N. E., S. R. Long, and L. F. Bliven, 1981: On the importance of the significant slope in empirical wind-wave studies. *J. Phys. Oceanogr.,* **11,** 569–571.

Hwang, P. A., 2007: Spectral signature of wave breaking in surface wave components of intermediate length scale. *J. Mar. Syst.,* **66,** 28–37, doi:10.1016/j.jmarsys.2005.11.015.

——, 2009: Estimating the effective energy transfer velocity at air-sea interface. *J. Geophys. Res.,* **114,** C11011, doi:10.1029/2009JC005497.

——, and D. W. Wang, 2004: An empirical investigation of source term balance of small scale surface waves. *Geophys. Res. Lett.,* **31,** L15301, doi:10.1029/2004GL020080.

——, and M. A. Sletten, 2008: Energy dissipation of wind-generated waves and whitecap coverage. *J. Geophys. Res.,* **113,** C02012, doi:10.1029/2007JC004277.

——, D. Xu, and J. Wu, 1989: Breaking of wind-generated waves: Measurements and characteristics. *J. Fluid Mech.,* **202,** 177–200.

——, D. W. Wang, E. J. Walsh, W. B. Krabill, and R. N. Swift, 2000: Airborne measurements of the directional wavenumber spectra of ocean surface waves. Part I: Spectral slope and dimensionless spectral coefficient. *J. Phys. Oceanogr.,* **30,** 2753–2767.

——, J. V. Toporkov, M. A. Sletten, D. Lamb, and D. Perkovic, 2006: An experimental investigation of wave measurements using a dual-beam interferometer: Gulf Stream as a surface wave guide. *J. Geophys. Res.,* **111,** C09014, doi:10.1029/2006JC003482.

——, M. A. Sletten, and J. V. Toporkov, 2008: Analysis of radar sea return for breaking wave investigation. *J. Geophys. Res.,* **113,** C02003, doi:10.1029/2007JC004319.

——, ——, and ——, 2010: A note on Doppler processing of coherent radar backscatter from the water surface: With application to ocean surface wave measurements. *J. Geophys. Res.,* **115,** C03026, doi:10.1029/2009JC005870.

Kasilingam, D. P., and O. H. Shemdin, 1988: Theory for synthetic aperture radar imaging of the ocean surface: With application to the Tower Ocean Wave and Radar Dependence Experiment on focus, resolution, and wave height spectra. *J. Geophys. Res.,* **93** (C11), 13 837–13 848.

Longuet-Higgins, M. S., 1985: Acceleration in steep gravity waves. *J. Phys. Oceanogr.,* **15,** 1570–1579.

——, and N. D. Smith, 1983: Measurement of breaking by a surface jump meter. *J. Geophys. Res.,* **88** (C14), 9823–9831.

Lyzenga, D. R., and J. R. Bennet, 1991: Estimation of ocean wave spectra using two-antenna SAR systems. *IEEE Trans. Geosci. Remote Sens.,* **29,** 1995–2002.

——, and N. P. Malinas, 1996: Azimuth falloff effects in two-antenna SAR measurements of ocean wave spectra. *IEEE Trans. Geosci. Remote Sens.,* **34,** 1020–1028.

Marom, M., R. M. Goldstein, E. B. Thornton, and L. Shemer, 1990: Remote sensing of ocean wave spectra by interferometric synthetic aperture radar. *Nature,* **345,** 793–795.

——, L. Shemer, and E. B. Thornton, 1991: Energy density directional spectra of a nearshore wave field measured by interferometric synthetic aperture radar. *J. Geophys. Res.,* **96** (C12), 22 125–22 134.

Phillips, O. M., 1984: On the response of short ocean wave components at a fixed wavenumber to ocean current variations. *J. Phys. Oceanogr.,* **14,** 1425–1433.

——, 1985: Spectral and statistical properties of the equilibrium range in wind-generated gravity waves. *J. Fluid Mech.,* **156,** 505–531.

——, and M. L. Banner, 1974: Wave breaking in the presence of wind drift and swell. *J. Fluid Mech.,* **66,** 625–640.

Plant, W. J., and W. C. Keller, 1983: The two-scale radar wave probe and SAR imagery of the ocean. *J. Geophys. Res.,* **88,** 9776–9784.

——, E. A. Terray, R. A. Petitt, and W. C. Keller, 1994: The dependence of microwave backscatter from the sea on illuminated area: Correlation times and lengths. *J. Geophys. Res.,* **99,** 9705–9723.

Romeiser, R., and D. R. Thompson, 2000: Numerical study on the along-track interferometric radar imaging mechanism of ocean surface currents. *IEEE Trans. Geosci. Remote Sens.,* **38,** 446–458.

Rosen, P. A., S. Hensley, I. R. Joughin, F. K. Li, S. N. Madsen, E. Rodriguez, and R. M. Goldstein, 2000: Synthetic aperture radar interferometry. *Proc. IEEE,* **88,** 333–382.

Sletten, M. A., 2006: An analysis of gradient-induced distortion in ATI-SAR imagery of surface currents. *IEEE Trans. Geosci. Remote Sens.,* **44,** 1995–2002.

Terray, E. A., M. A. Donelan, Y. C. Agrawal, W. M. Drennan, K. K. Kahma, A. J. Williams, P. A. Hwang, and S. A. Kitaigorodskii, 1996: Estimates of kinetic energy dissipation under breaking waves. *J. Phys. Oceanogr.,* **26,** 792–807.

Thompson, D. R., and J. R. Jensen, 1993: Synthetic aperture radar interferometry applied to ship-generated internal waves in the 1989 Loch Linnhe Experiment. *J. Geophys. Res.,* **98** (C6), 10 259–10 269.

Tiessen, M. C. H., N. Dodd, and R. Gamier, 2011: Development of crescentic bars for a periodically perturbed initial bathymetry. *J. Geophys. Res.,* **116,** F04016, 10.1029/2011JF002069.

Toba, Y., 1973: Local balance in the air–sea boundary processes. Part III: On the spectrum of wind waves. *J. Phys. Oceanogr.,* **3,** 579–593.

Toporkov, J., D. Perkovic, G. Farquharson, M. A. Sletten, and S. J. Frasier, 2005: Sea surface velocity vector retrieval using dual-beam interferometry: First demonstration. *IEEE Trans. Geosci. Remote Sens.,* **43,** 2494–2502.

Vachon, P. W., J. W. M. Campbell, A. L. Gray, and F. W. Dobson, 1999: Validation of along-track interferometric SAR measurements of ocean surface waves. *IEEE Trans. Geosci. Remote Sens.,* **37,** 150–162.

Walsh, E. J., D. W. Hancock, D. E. Hines, R. N. Swift, and J. F. Scott, 1985: Directional wave spectra measured with the surface contour radar. *J. Phys. Oceanogr.,* **15,** 566–592.

——, ——, ——, ——, and ——, 1989: An observation of the directional wave spectrum evolution from shoreline to fully developed. *J. Phys. Oceanogr.,* **19,** 670–690.

Zhang, B., W. Perrie, and Y. He, 2009: Remote sensing of ocean waves by along-track interferometric synthetic aperture radar. *J. Geophys. Res.,* **114,** C10015, doi:10.1029/2009JC005310.